The Mesoscale Dynamics of Freezing Rain Storms over Eastern Canada

K. K. SZETO

Climate Processes and Earth Observation Division, Atmospheric Environment Service, Downsview, Ontario, Canada

A. TREMBLAY

Cloud Physics Research Division, Atmospheric Environment Service, Dorval, Quebec, Canada

H. GUAN AND D. R. HUDAK

Cloud Physics Research Division, Atmospheric Environment Service, Downsview, Ontario, Canada

R. E. STEWART AND Z. CAO

Climate Processes and Earth Observation Division, Atmospheric Environment Service, Downsview, Ontario, Canada

(Manuscript received 2 June 1997, in final form 9 June 1998)

ABSTRACT

A severe ice storm affected the east coast of Canada during the Canadian Atlantic Storms Project II. A hierarchy of cloud-resolving model simulations of this storm was performed with the objective of enhancing understanding of the cloud and mesoscale processes that affected the development of freezing rain events. The observed features of the system were reasonably well replicated in the high-resolution simulation. Diagnosis of the model results suggests that the change of surface characteristics from ocean to land when the surface warm front approaches Newfoundland disturbs the (quasi-) thermal wind balance near the frontal region. The cross-frontal circulation intensifies in response to the thermal wind imbalance, which in turn leads to the development of an extensive above-freezing inversion layer in the model storm. Depending on the depth of the subfreezing layer below the inversion, the melted snow may refreeze within the subfreezing layer to form ice pellets or they may refreeze at the surface to form freezing rain. Such evolution of surface precipitation types in the model storm was reasonably well simulated in the model. Model results also show that the horizontally differential cooling by melting near the nose of the above-freezing inversion layer enhances the local baroclinicity, which in turn induces perturbations on the cross-front flow. Depending on stability of the ambient flow, such local flow perturbations may trigger symmetric or convective overturning above the region and consequently enhance the local precipitation production via a positive feedback mechanism.

1. Introduction

One of the most challenging tasks facing a weather forecaster is the prediction of surface precipitation types within midlatitude winter storms. For example, the form of precipitation becomes difficult to predict whenever the surface temperature approaches 0°C. Precipitation in the form of snow, ice pellets,[1] freezing rain,[2] and rain can occur simultaneously within the vicinity of the rain–snow boundary (see, e.g., Stewart 1992; Stewart et al. 1995, among others). Among these forms of winter precipitation, freezing rain is the most dangerous and the most difficult to forecast. The icy surface conditions during an ice storm can severely disrupt ground activities and the accumulation of ice on electrical transmission facilities can lead to the interruption of power transmission. For example, millions of families were cut off from electricity supply for prolonged periods (some up to several weeks) during the devastating ice storms that occurred over the Ottawa–Montreal regions of Canada during early January 1998, putting the major metropolitan regions into a state of emergency and resulting in hundreds of millions of dollars of insurance costs.

While a comprehensive global climatology of ice storms is not known to the authors, freezing rain is generally restricted to the temperate zones above about 35°N. In general, the occurrence of freezing rain in these

[1] *Ice pellet:* Precipitation consisting of transparent or translucent pellets of ice that have formed from the freezing of rain or refreezing of largely melted snowflakes (Huschke 1959).

[2] *Freezing rain:* Rain that falls in liquid form but freezes upon impact to form a coating of glaze upon the ground and on exposed objects (Huschke 1959).

Corresponding author address: Kit K. Szeto, CCRP, AES, 4905, Dufferin Street, Downsview, ON M3H 5T4, Canada.
E-mail: kit.szeto@ec.gc.ca

regions is not frequent. For example, the major metropolitan regions from Washington to Boston average only 10 h of freezing precipitation per winter (Knight 1996) and freezing rain occurs occasionally over Europe and other regions (see, e.g., Pike 1995). However, there are also regions that are particularly prone to the occurrence of freezing precipitation during the winter. The Avalon peninsula of Newfoundland, Canada, is one of those regions that experiences frequent and severe ice storms. For example, during the 2 months (15 January–15 March 1992) of the Canadian Atlantic Storms Program (CASP II) field project (Stewart 1991), freezing rain was observed in 11 out of the 16 storms that occurred over the region. In fact, one of the prime objectives of the CASP II project was to investigate the nature of these freezing rain storms.

The general attributes of freezing rain and ice pellets as well as the background synoptic conditions associated with these storm events are certainly known (see Stewart 1992 for a general review of earlier research on this topic). Basic requirements for the formation of freezing precipitation through ice phase mechanisms include an above-freezing inversion layer (AFIL) at the low levels and subfreezing surface temperatures (for the sake of simplicity, the term AFIL will be used to denote an above-freezing inversion layer overlying a surface layer of air at subfreezing temperatures in the following discussions). Such low-level inversion layers are often associated with surface fronts. However, the dynamic processes that lead to the enhancement or destruction of the AFIL are not well understood. In addition, the melting of snow particles in the AFIL and their subsequent refreezing at the lower levels or at the surface can induce differential diabatic cooling–heating in the vertical, and the dynamic consequences of these processes have not been thoroughly studied.

Traditionally, the prediction of surface precipitation type has relied upon atmospheric thickness techniques (Lamb 1955; Bocchieri 1980). More recently, additional thermal variables have been included in the predictor list (Heppner 1992; Erickson et al. 1993). However, such techniques are still incapable of accounting for effects of the critical finescale structure of the precipitation that results from the complex physical processes occurring in the transition region. For example, Donaldson and Stewart (1993) and Crawford and Stewart (1995) showed that the production of freezing rain and ice pellets depends on the temperature structure and particle characteristics aloft. Hanesiak and Stewart (1995) even found that the reduction of snow melting due to evaporative cooling inside a subsaturated region induced by subsiding air within an inversion was partly responsible for a prolonged period of ice pellets during the passage of a Canadian Atlantic winter storm.

On the modeling side, several recent studies have investigated winter precipitation processes and their impacts on the parent storm. For example, Gedzelman and Arnold (1993) simulated the various forms of precipitation within winter storms by using a kinematic 2D cloud model and investigated the thermal impacts associated with the transition of the precipitation types on the parent storms. The effects of evaporation and melting on the development of frontal rainbands have also been investigated numerically by Barth and Parsons (1996). By using a 2D full prognostic cloud model, the sequence of surface weather elements ahead of the warm fronts of winter cyclones as observed by Stewart et al. (1995) was quite successfully simulated by Szeto and Stewart (1997a). In addition, Szeto and Stewart (1997b) showed that cooling by melting in the lower levels can accelerate surface frontogenesis, while cooling by melting in the midtroposphere can aid or lead to the formation of banded precipitation features. However, the full consequences of the coupling between the precipitation processes and the dynamics of the parent storm as well as the effects of the storm environment on the development of these weather events were not well replicated in these simulations due to the constraints inherent to these simpler models.

One freezing rain storm occurred on 26 February 1992 during intensive observation period (IOP) 13 of CASP II. This storm deepened rapidly and it passed over the Avalon peninsula of Newfoundland where it was well sampled with a variety of observational platforms (Hudak et al. 1996, hereafter referred to as HSTL). In this present paper, the mesoscale structure of the 26 February storm is investigated with a hierarchy of 3D numerical simulations. Although several numerical studies have been conducted on rapidly deepening oceanic extratropical cyclones (e.g., Kuo et al. 1991; Chang et al. 1993, among many others), the present study is unique in that a reasonably high horizontal model resolution (10 km) and a quite sophisticated cloud microphysics scheme (for the current standards of 3D cyclone simulations) including ice-phase processes are employed in some of the simulations. The degree to which the observed cloud and mesoscale structures of the system can be replicated in the cloud-resolving simulations will be assessed. The model results will then be diagnosed to examine the physical processes affecting the organization and forms of precipitation ahead of the surface warm front of this storm. In particular, the processes leading to the occurrence of a prolonged freezing rain episode during the passage of the storm will be examined.

The article is organized as follows. A summary is first given of the nature of the system, a brief description of the Mesoscale Compressible Community (MC2) model and results of a number of model simulations of this case are then given and compared against observations. This is followed by a discussion of the processes responsible for some of the observed and simulated internal structures of the system.

2. Observations

A detailed observational analysis of the case is given in HSTL and only a brief summary of the observed

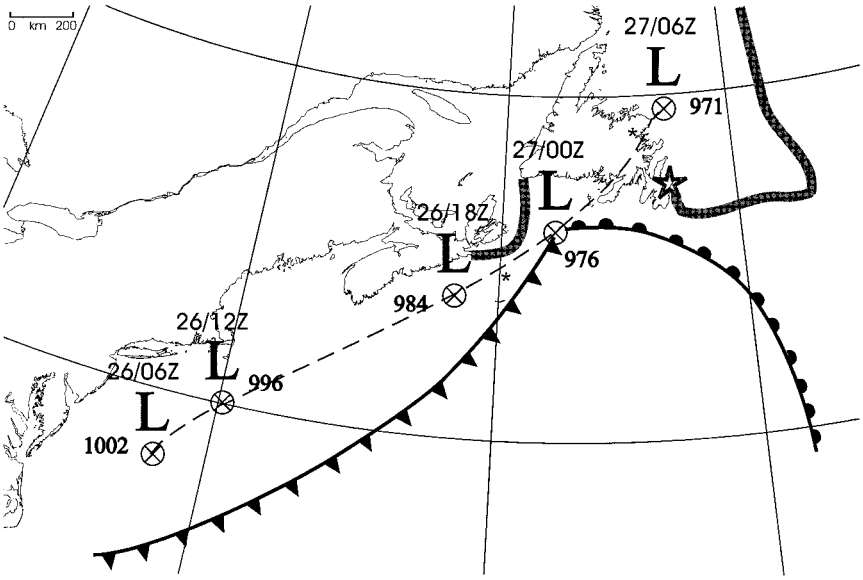

FIG. 1. The track of the low and frontal positions during IOP 13 on 26–28 February 1992. Times are given above the low center. The thick shaded line indicates the approximate sea ice edge. The area over which the observations on the Avalon peninsula were taken is indicated by a star.

evolution and structure of the storm will be presented here.

a. Background synoptic conditions

A rapidly deepening cyclone was moving up the east coast of North America during IOP 13 (26–27 February 1992) of CASP II (Fig. 1). The central pressure of the low fell 31 hPa in 24 h and the warm front associated with this system approached the Avalon peninsula (see Fig. 4b for a map of the geographical locations referred to in this paper) at around 0000 UTC 27 February. In the 6 h (1800 UTC 26 February to 0000 UTC 27 February) during which most of the precipitation fell over the Avalon peninsula, the low deepened 8 hPa. Virtually all of the precipitation that totaled 17.5 mm of liquid equivalent at St. John's was ahead of the warm front. After 0000 UTC 27 February the occlusion process began as the low tracked across central Newfoundland. The crest of the frontal wave passed just northwest of the Avalon peninsula.

The CASP II area was downstream of a major 500-hPa trough centered over the Great Lakes. However, there was no strong vorticity advection at this level associated with the surface low. At 250 hPa the position of the jet stream was such that the surface low moved into a strongly divergent region in the upper levels. This was a major factor in the rapid deepening process of the cyclone.

b. Precipitation structure

The main precipitation area, which passed over the Avalon peninsula between about 2000 UTC 26 February and 0000 UTC 27 February, was in the form of banded structures (features B1–B3 in Fig. 2) oriented parallel to the warm front. The second band (B2) was the main feature of interest because the transition of surface precipitation type was observed to accompany the passage of this band over the region. During the passage of band B2 a number of narrow ($\sim$2 km) reflectivity cores (with $Z_e > 30$ dBZ) passed over Torbay. Such narrow structures were not resolved by the Holyrood radar (Fig. 2b) but they were clearly detected by the Doppler radar located at Torbay (see Fig. 6 of HSTL). These cores were oriented perpendicular to the main band and were 5–10 dBZ higher in intensity than the rest of the band. Such perpendicular high reflectivity cores were not observed in the first band (B1) passed over the region. A low-level jet with a double jet core structure was observed to accompany the occurrence of these precipitation cores, which were oriented perpendicular to the front (see Fig. 3 of HSTL). The band possessed a slight arc-shaped structure (with the vertex near the location of the letters ''B2'' in Fig. 2b). In the vicinity of the second band, between 1.0- and 1.5-km levels there were significant horizontal disturbances in the temperature fields constructed from aircraft and radiosonde data (see Fig. 8 of HSTL). These temperature perturbations (reflected locally as regions of enhanced or reduced baroclinicity) distorted the uniformly sloping frontal surface typically depicted on the synoptic scale. They coincided with the appearance of the 0°C level in the vertical temperature profile, suggesting that processes associated with melting and refreezing had some influence on the overall dynamics.

During the passage of the third band (B3), 2-km-deep

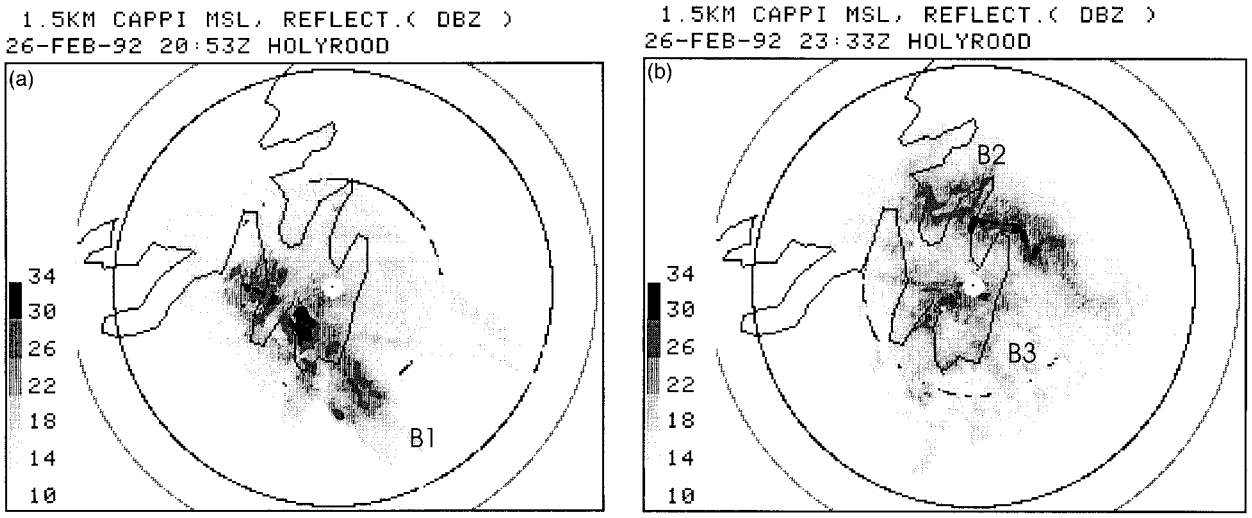

FIG. 2. CAPPIs of reflectivity in dBZe at 1.5 km deduced from the Holyrood radar at (a) 2053 UTC and (b) 2333 UTC 26 February 1992. B1, B2, and B3 indicate banded precipitation features discussed in the text and the range rings are shown at 100 km. (Adapted from Hudak et al. 1996.)

higher-reflectivity cores were also observed by the Doppler radar (see Fig. 10 of HSTL). However, in this band the cores were oriented parallel to the band and front. The vertical velocity and turbulence measured by the research aircraft (see Figs. 7b and 7c of HSTL) as well as the relatively high liquid water contents in the region suggest that these cores were results of embedded convection within band B3.

The changes of surface precipitation accompanying the passage of the system over the region are presented in Fig. 3. During the passage of band B2, surface precipitation evolved from large snowflakes and heavily rimed particles to a mixture of snow and ice pellets and then ice pellets and freezing rain. Freezing rain/drizzle occurred mainly in the lighter precipitation region between the cores of bands B2 and B3 and only rain and drizzle were associated with band B3. The ice pellets lasted for about 2 h and the freezing rain lasted for about

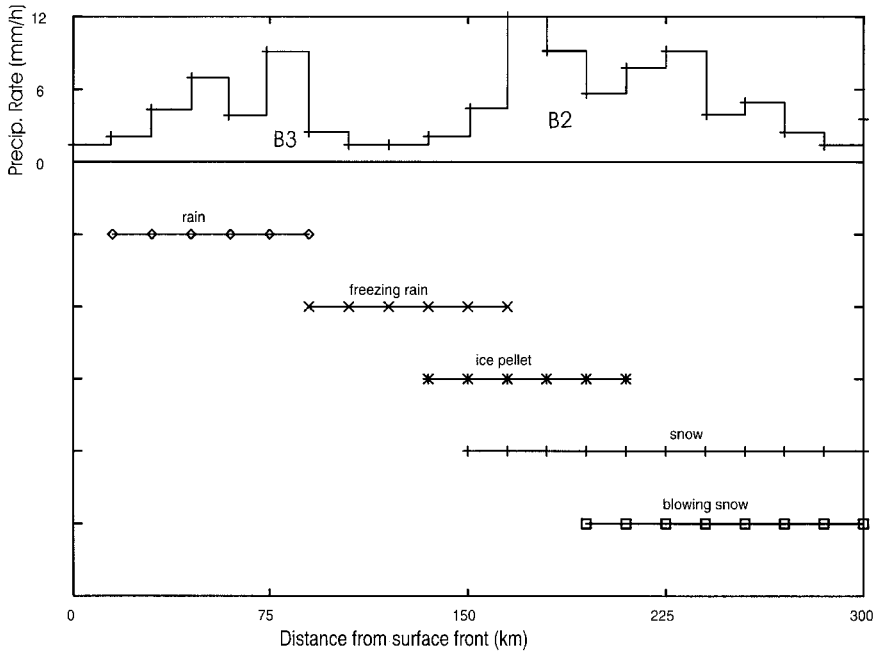

FIG. 3. Distribution of precipitation rate and types observed at St. John's airport during the passage of the storm. B2 and B3 indicate banded precipitation features corresponding to the ones depicted in Fig. 2.

2.5 h at St. John's airport. Last, it is noteworthy that the heaviest precipitation ($\sim$12 mm h^{-1}) occurred during the period of ice pellets/snow.

In summary, the observed intensive cyclone possessed complex but organized structures in its warm-frontal cloud and precipitation fields. An intense and prolonged ice pellets/freezing rain event occurred during the passage of one of the stronger bands over the region. In the next section, we will make use of cloud model results to investigate the processes responsible for the observed organized structures within this storm.

3. Model description and simulations

The model used in this work is the fully compressible, semi-implicit semi-Lagrangian (SISL), three-dimensional, nonhydrostatic MC2 model. Some characteristics of the model include variable vertical resolution, modified Gal-Chen terrain following vertical coordinate, limited-area one-way nesting capability, and a complete physics package including several cloud schemes of various degrees of sophistication and a turbulence kinetic energy boundary layer parameterization scheme (Benoit et al. 1989). The novel SISL dynamical framework employed in this model makes it quite unique among existing nonhydrostatic models. The model has been used successfully to study a wide spectrum of phenomenon ranging from microscale supersonic waves and finescale bubble convection, to mesoscale features such as squall lines (e.g., Tremblay 1994), frontal cloud systems (e.g., Tremblay et al. 1995), and synoptic-scale systems (e.g., Kong and Yau 1997), demonstrating the versatility of the SISL dynamical framework. A complete description of the model can be found in Tanguay et al. (1990) and Benoit et al. (1997).

A series of model runs were carried out at horizontal resolutions appropriate for large scales (50 km grid length), the meso-β (25 km), and the meso-γ scale (10 km) (Fig. 4). A 36-h simulation was performed from 26 February at 0000 UTC until 27 February at 1200 UTC for the 50-km run. The simulation periods were 24 and 12 h starting at 0000 UTC 26 February and 1200 UTC 26 February for the 25- and 10-km runs, respectively. With 33 vertical Gal-Chen levels and a 18-km model lid, the smallest vertical grid size is 250 m in the lower atmosphere (up to 5 km above ground level) and the largest is 2000 m near the top of the domain in all simulations.

In the 50-km grid length simulation (KUOSUND50), the domain sizes are 7750 km in the east–west direction and 6050 km in the north–south direction. Canadian Meteorological Centre analysis data were used to initialize the model, and a combination of the Kuo (1974) cumulus parameterization and the Sundqvist et al. (1989) condensation scheme was used. The Sundqvist scheme involves a single prognostic equation for cloud water and there is no ice microphysics. This scheme is used quite commonly in GCMs and large-scale forecast models. The time step is 360 s.

The output from the 50-km simulation was then used to provide the boundary conditions to a 25-km run (KUOSUND25), employing the same model physics as in large-scale simulation. For this next run, the horizontal domain is 4025 km (161 grid points) and 3525 km (141 grid points), respectively. The time step is 180 s.

The output from the 25-km run was used to provide initial and boundary conditions for the 10-km simulation (BULKMIC10). For this simulation, the domain size is 1810 km in the east–west direction and 1610 km in the north–south direction (Fig. 4). The time step is 120 s. No moist convection parameterization was used in this simulation. The bulk water cloud microphysics scheme of Kong and Yau (1997) was employed in BULKMIC10. The version of this microphysics scheme employed in this simulation includes three prognostic equations for cloud water content, rainwater content, and the ice phase.

To examine the bulk effects of the ice phase processes, a simulation (WARM_RAIN) was performed with configurations similar to experiment BULKMIC10 but with only the warm rain physics in the Kong–Yau scheme being switched on. An additional experiment (NO_TOPO) was carried out similar to BULKMIC10 but with the topography removed in the model to study the effects of topographic features on the model results. Results from other sensitivity runs will also be discussed where appropriate.

4. Model results

a. The KOUSUND50 simulation

Figure 5 shows the positions and magnitudes of the mean sea level pressure centers of the observed and simulated storms. The track of the simulated storm shows good agreement with the observed one. While the deepening rate of the model low pressure system was slightly slower than that of the observed system in the earlier stage of the simulation, both the pressure and the location of the low center agreed well with observations at the end of the simulation. Both the actual and the simulated warm fronts passed over the Avalon peninsula near 0000 UTC 27 February. Since the main purpose of this run is to provide time-dependent lateral boundary conditions for the 25-km resolution experiments, results from this simulation will not be discussed further.

b. The KOUSUND25 simulation

To compare the mesoscale precipitation structures within the warm front against observations and results from other experiments, the simulated surface isobars and precipitation rates near Newfoundland at 0000 UTC 27 February are shown in Fig. 6. The location of the

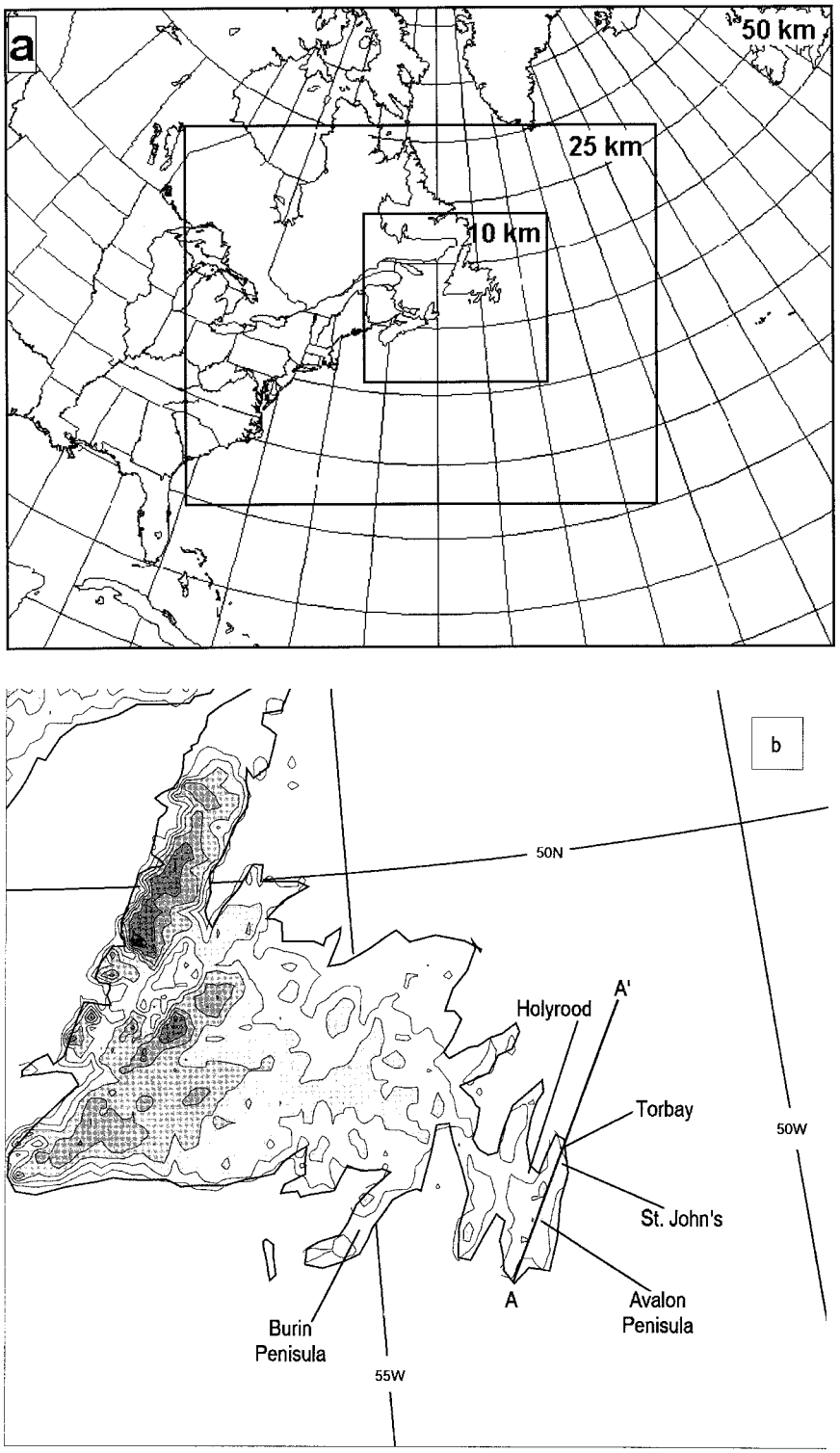

FIG. 4. (a) Domains of the three simulations. (b) A blowup of the subdomain near Newfoundland showing the topography (at 100-m shading intervals) as well as the line (AA′) where the cross sections of model results will be shown at 0000 UTC 27 February.

FIG. 5. Observed and simulated storm track from the KUOSUND50 run.

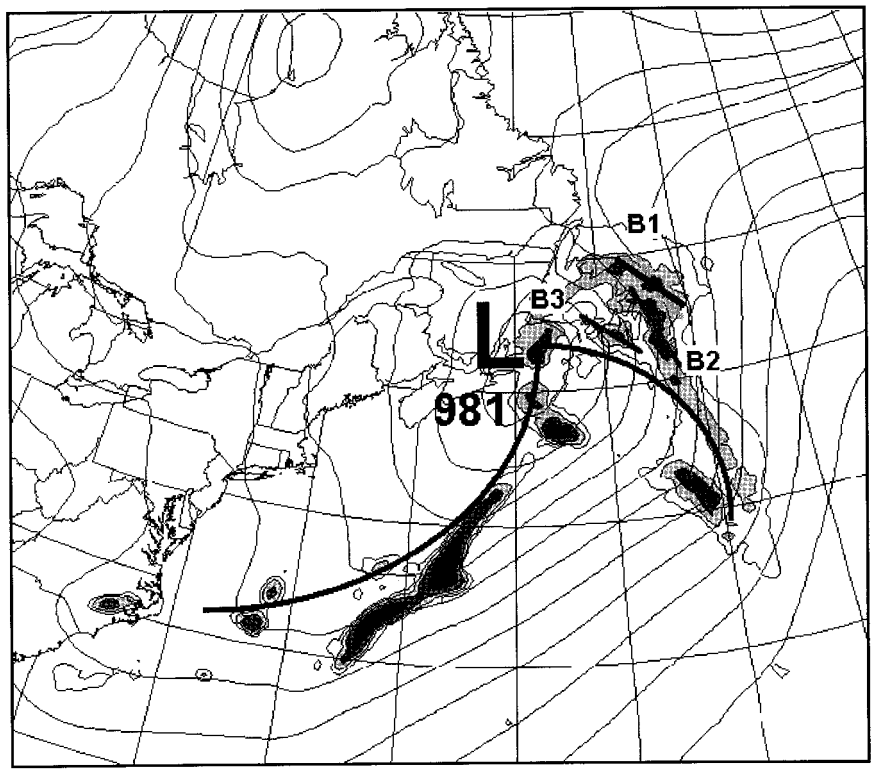

FIG. 6. Surface precipitation rate (at 2 mm h^{-1} shading intervals) and surface isobars (4-kPa intervals) for the KUOSUND25 simulation at 0000 UTC 27 February. The three warm frontal bands are annotated by B1–B3 and the location of the surface low center and frontal zones are also indicated.

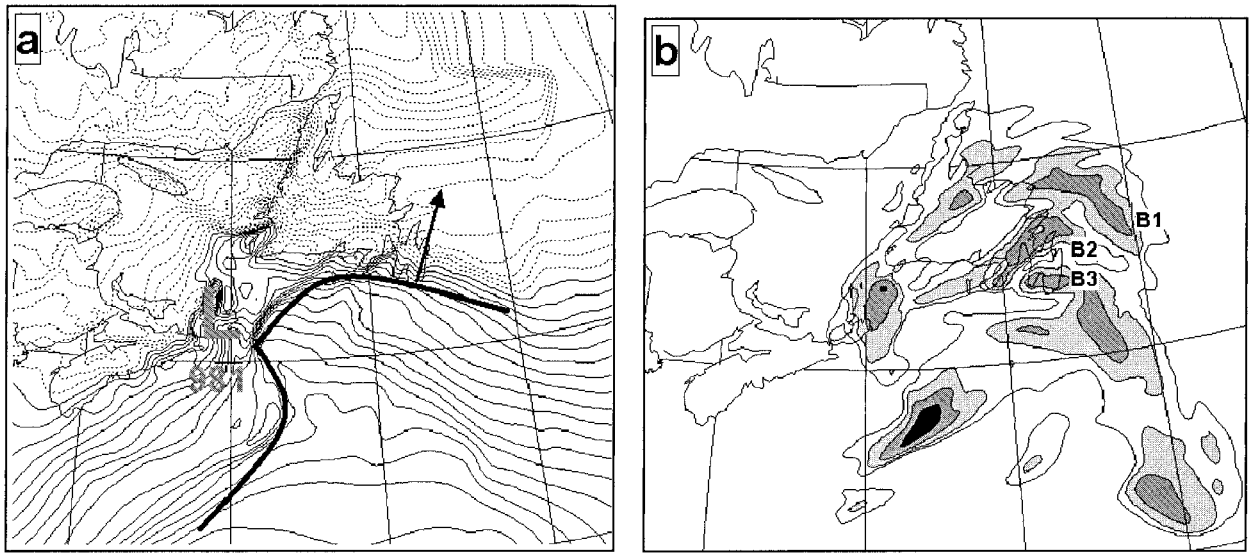

FIG. 7. Results for simulation BULKMIC10 at 0000 UTC 27 February. (a) Surface isotherms (at 1°C intervals with dashed lines indicating subfreezing values). Also indicated are the low center, the frontal positions, and the line AA′. (b) Surface precipitation rate (at 2 mm h^{-1} shading intervals).

surface low center in the model is close to the observation, although the pressure at the observed low center is 5 mb lower. The strongest precipitation rates are found near the cold front (maximum of 18.5 mm h^{-1}). Three warm-frontal precipitation bands are evident near the Avalon peninsula. They are all nearly parallel to the warm front and their width is about 75 km. Similar to observations, the highest precipitation rate is found in the core of band B2. However, the maximum precipitation rate of 6.5 mm h^{-1} is significantly lower than that observed over the region (~12 mm h^{-1}) and the embedded precipitation cores are located off the east coast of Newfoundland while they were observed over northern Avalon peninsula at 0000 UTC 27 February (Fig. 2b). In addition, band B1 is a bit (~40 km) too close to the peninsula and band B3 is located just south of the peninsula instead of over the peninsula as in the observations (Fig. 2). The location of the surface warm frontal zone near the peninsula is similar to observations but the frontal intensity is slightly weaker than the observed values [~4.3 vs 6 K $(100\ km)^{-1}$; see Fig. 8 of HSTL].

Accumulated precipitation of up to about 13 mm was obtained near St. John's and, similar to the observations, most of this occurred over the 6-h period starting at 1800 UTC 26 February. These model-generated precipitation values were less than the observed value (~17.5 mm).

c. The BULKMIC10 simulation

Model outputs from the BULKMIC10 simulation are presented in Figs. 7–10. Figures 7a,b show the near-surface temperatures and precipitation rates of the model storm at 0000 UTC 27 February. It can be noted that the surface warm front has just reached the Avalon peninsula at that time, similar to observations. The intensity of the surface warm-frontal zone over the Avalon peninsula is stronger than that in the KUOSUND25 simulation [~4.3 K $(100\ km)^{-1}$] and is more comparable to observations [both at ~6 K $(100\ km)^{-1}$; see Fig. 8 of HSTL].

Similar to observations and the results of the KUOSUND25 simulation, three precipitation bands (B1, B2, and B3) were formed ahead of the surface warm front. When compared to the KUOSUND25 results, the maximum precipitation rates are slightly higher in the BULKMIC10 case (~8 vs ~6.5 mm h^{-1}) and the values are in slightly better agreement with observations (~12 mm h^{-1}). The locations, orientations, and core structures of the bands B1 and B3 are also more in agreement with observations. In particular, band B1 is now located more to the north to agree with its observed location at 0000 UTC 27 February and band B3 is now located over central Avalon as in the observations (Fig. 2).

Although the main precipitation cores in B2 are over the peninsula (instead of being located over the ocean off the east coast of the peninsula in KUOSUND25), band B2 exhibits an overall NE–SW-oriented structure instead of the overall NW–SE-orientation band structures of B2 in the observations (Fig. 2b) and in KUOSUND25. An ''arching'' of the band yielding a short extension of the band in the NW–SE direction is evident at the northern edge of the peninsula. Effects of topography (there are numerous shallow and narrow ranges aligned roughly along the ''fingers'' of the peninsula; see Fig. 4b) on the model precipitation field are evident. For example, the strongest precipitation cores in band

B2 are located on the upwind side of the ranges and extend southwestward over the peninsula. The southwestward extension of the observed band B2 was only weakly evident in the radar display (Fig. 2b), but it should be noted that the southwest end of the peninsula is outside of the reliable range of the Holyrood radar. It is of interest to note that the corresponding bands in simulations KUOSUND25 (where the narrow topographic features are not resolved) and NO_TOPO (where the topography is totally removed) are aligned in the NW–SE direction as in the observations, suggesting that effects of these small-scale topographic features are not handled well with the resolution used in the present simulation.

Cross sections of several meteorological fields from case BULKMIC10 at 1800 UTC 26 February and 0000 UTC 27 February are given in Figs. 8 and 9, respectively. The cross sections are chosen to be perpendicular to the surface warm front with the origin location near the front (the location of the cross section at 0000 UTC 27 February is shown along line AA′ in Fig. 4b, corresponding to the location of the cross-sectional analysis presented in HSTL; corresponding cross sections with respect to the location of the surface warm front are used at 1800 UTC 26 February). A Cartesian coordinate with the x axis aligned along the front and the y axis pointing toward the cold side of the warm front will be used in the following discussions.

The vertical thermodynamic structure of the warm-frontal zone (Figs. 8a,b and 9a,b) is typical of this kind of storm over the region. The surface frontal transition zone is about 130 km wide, similar to other cases observed over eastern Canada by Taylor et al. (1993). Average strength of the surface warm front increases from $\sim$4.5 K (100 km)$^{-1}$ at 1800 UTC 26 February to $\sim$6.5 K (100 km)$^{-1}$ at 0000 UTC 27 February. The model front moved at an average speed of $\sim$12.5 m s^{-1} over the 6 h. Both the frontal strength and frontal speed are similar to observations. A strong low-level frontal inversion is the most notable feature in the temperature field (Figs. 8a and 9a). The width of the above-freezing inversion layer (the distance between the surface 0°C isotherm and northern tip of the above-freezing inversion layer) increases from $\sim$37 km at 1800 UTC 26 February to $\sim$180 km at 0000 UTC 27 February. The structure of the inversion layer at 0000 UTC 27 February is very similar to that of the observed case (see Fig. 8 in HSTL). This strong above-freezing inversion layer is responsible for the mixed-phase precipitation at the surface in both the observed and modeled storms.

Further details of the developing frontal zone are revealed in the equivalent potential temperature θ_e and $\partial\theta_e/\partial y$ fields (Figs. 8b,c and 9b,c). As expected, strong stability to vertical displacements is found within the frontal zone while conditions are near neutral or slightly unstable to saturated ascents above the frontal zone. An interesting feature in the θ_e field at 0000 UTC 27 February is found near the nose of the above-freezing inversion layer (marked ''M'' in Figs. 9b,c) where a sharp step change in the 310-K moist isentrope occurs as a result of enhanced $\partial\theta_e/\partial y$ in the region. Step changes in the frontal zone are also revealed in the $\partial\theta_e/\partial y$ fields at both model times as regions of enhanced frontal contrast along the sloping frontal zone (Figs. 8c and 9c). The intensities of these perturbations are much stronger at 0000 UTC 27 February and the wavelength of these perturbations on the frontal zone is $\sim$75 km at 0000 UTC 27 February. ''Staircase'' structures are inferred in the observed front and, in particular, the sharp step change at the upper frontal zone near the nose of the AFIL was clearly analyzed in the observed data (see Fig. 8 of HSTL).

The vertical velocity fields across the frontal zone at 1800 UTC 26 February and 0000 UTC 27 February are shown in Figs. 8d and 9d, respectively. The vertical velocities are generally much stronger at 0000 UTC 27 February. Enhanced updrafts (WF and W3 in Fig. 9d) above the surface front are apparent at both times, presumably in association with enhanced low-level frontal convergence over the region. A quite strong and deep downdraft occurs at $\sim$100 km from the surface front at 0000 UTC 27 February. This downdraft is not evident at 1800 UTC 26 February but it was measured by the CASP II research aircraft (see Fig. 6 of HSTL). Farther ahead into the cold sector, enhanced updraft regions embedded within the frontal upglide are evident at both times. In general, these updraft cores are found near the regions of enhanced frontal contrast mentioned earlier. However, a deep updraft cell (W2) located near the nose of the above-freezing inversion at 0000 UTC 27 February has no counterpart found at 1800 UTC 26 February. Weak sinking motions beneath the frontal zone start at $\sim$180 and $\sim$300 km ahead of the surface front at 1800 UTC 26 February and 0000 UTC 27 February, respectively. Due to the extensive region of low-level updraft at 0000 UTC 27 February, the whole subdomain presented in Fig. 9 is at or near saturation.

The cross-front (v) and alongfront (u) velocities at the two different times are shown in Figs. 8e,f and 9e,f, respectively. It is of interest to note that although the low-level frontal contrast increased by 40% during the 6 h from 1800 UTC 26 February to 0000 UTC 27 February, the strength of the alongfront jet (J1) only increased slightly (with the maximum alongfront wind increasing from 22 to 24 m s^{-1}) over the period (Figs. 8f and 9f). In contrast, the intensity of the cross-front flow increased significantly and a jet core (J2) with front-relative $v > 25$ m s^{-1} is found near the 1.5-km altitude at 0000 UTC 27 February (Figs. 8e and 9e). These low-level jet cores in u and v form a double jet structure in the model wind field quite similar to that in the observed storm (see Fig. 3 of HSTL).

Cross sections of the modeled precipitation fields are presented in Figs. 8g,h and 9g,h. It is clear that two banded precipitation features (B2 and B3 in Fig. 9h) associated with the enhanced updraft regions (W2 and

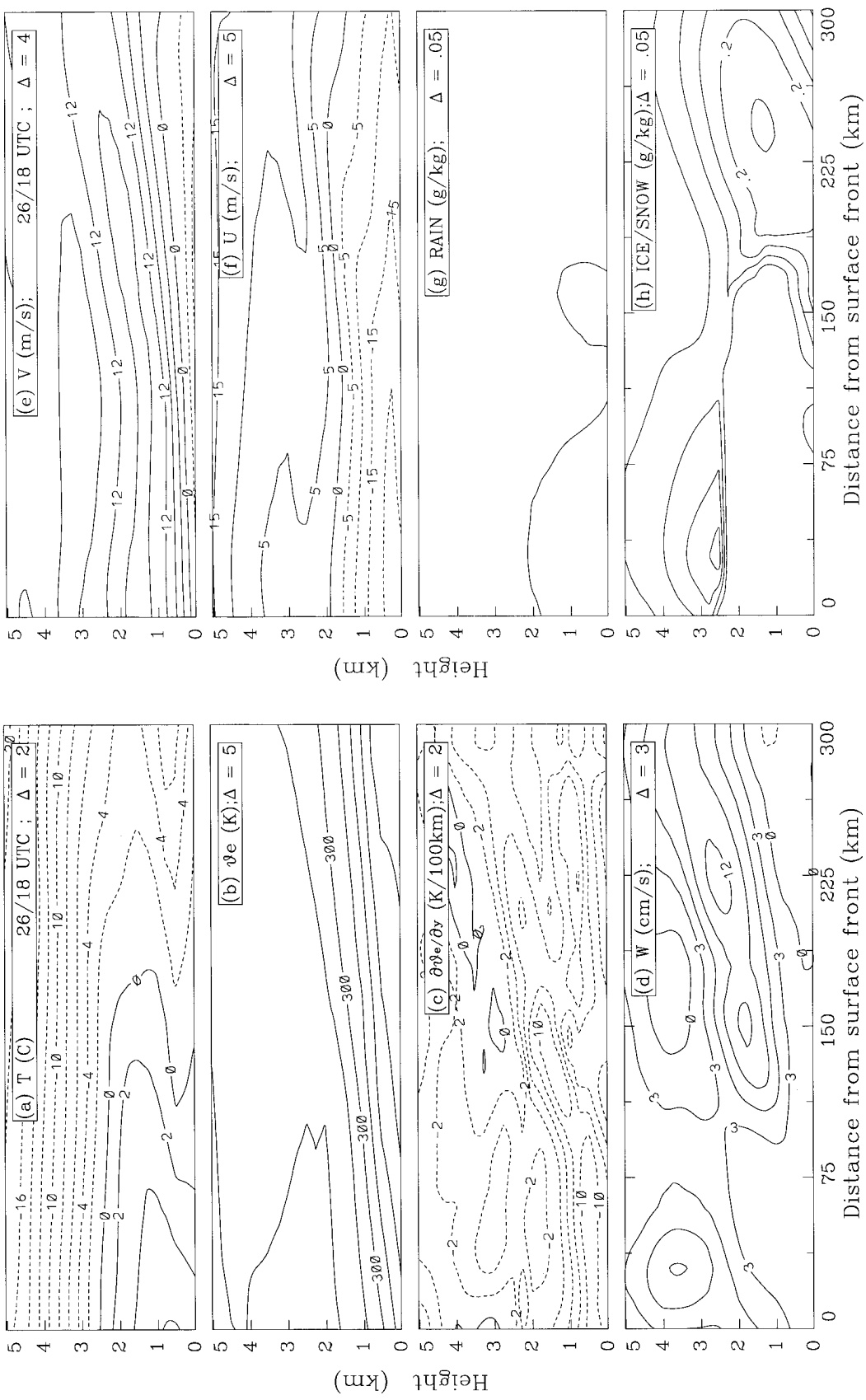

FIG. 8. Cross sections of various fields along line AA′ at 1800 UTC 26 February from the BULKMIC10 simulation: (a) temperature, (b) equivalent potential temperatures, (c) horizontal gradients of equivalent potential temperatures, (d) vertical velocities, (e) front-relative cross-front velocities, (f) alongfront velocities, (g) rain mixing ratio, and (h) ice/snow mixing ratio. Units and contour intervals are given in the informational boxes.

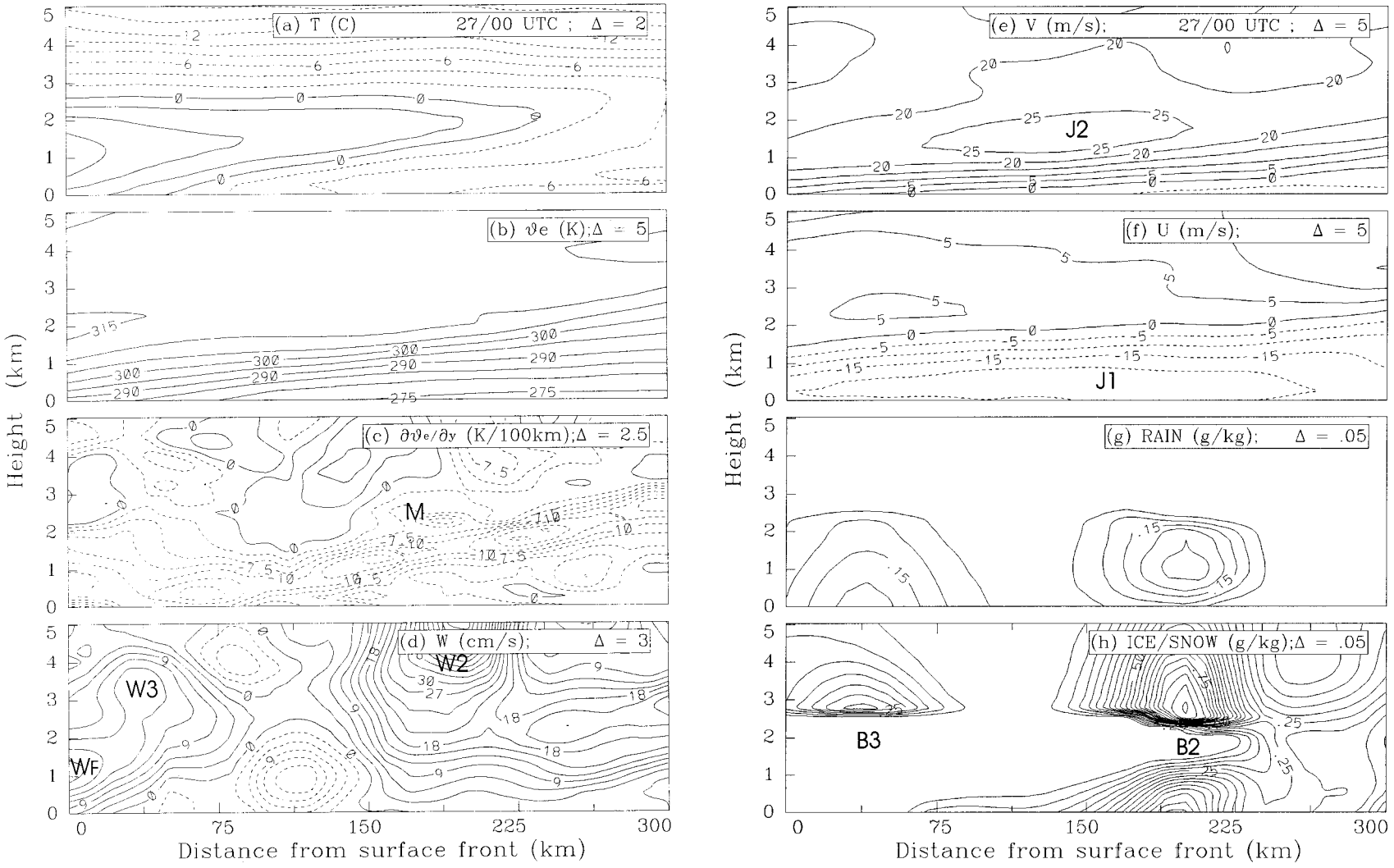

FIG. 9. As in Fig. 8 but at 0000 UTC 27 February.

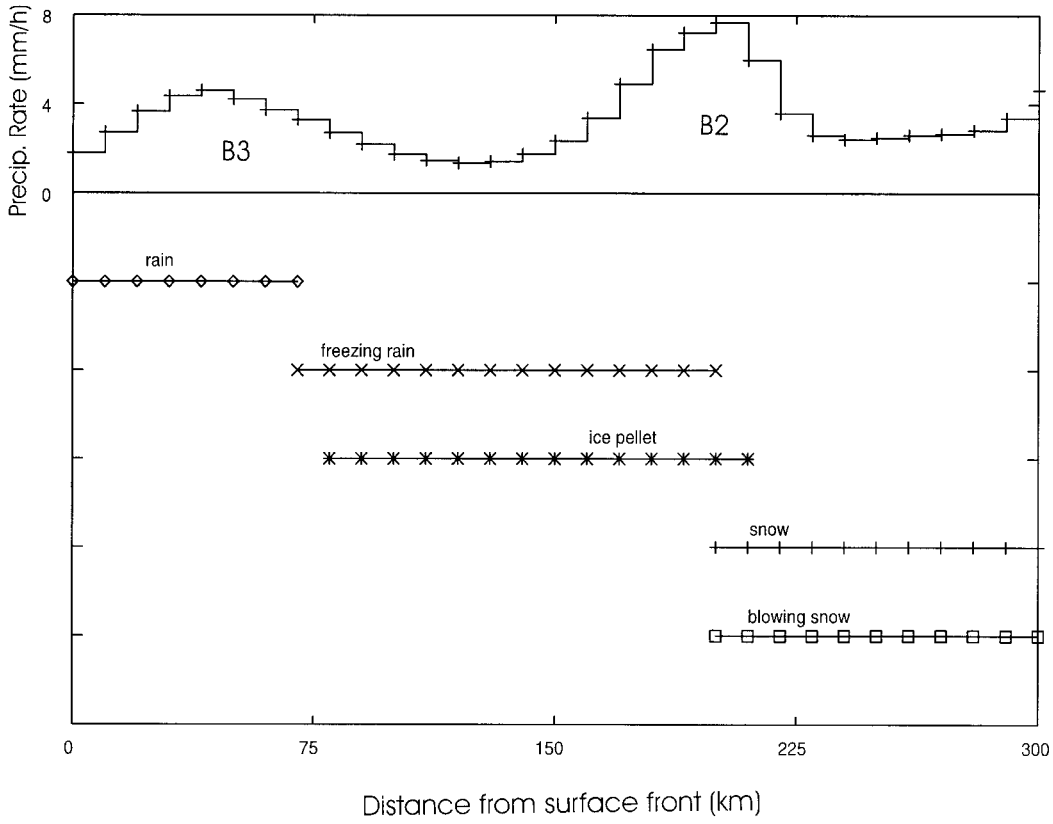

FIG. 10. Distribution of surface precipitation rate and types along line AA′ at 2700 UTC for the BULKMIC10 simulation.

W3) discussed earlier are present in this subdomain of the model storm. At 1800 UTC 26 February, the two bands are quite weak and snow changes to rain in a simple fashion at the surface due to the absence of a strong AFIL layer at this time. At 0000 UTC 27 February, the precipitation is much stronger. The width (~75 km) and separation of the two modeled precipitation bands agree extremely well with those in the observed case. Above the melting level, the precipitation was in the form of snow. The snow melted to form rain in the above 0°C region of the inversion layer and some of the rain refroze to the solid phase in the surface subfreezing layer (Figs. 9g,h), leading to the formation of a broad precipitation phase transition zone at the surface.

Using the criteria adopted in Szeto and Stewart (1997a), the surface precipitation type can be diagnosed from the model results (Fig. 10). Freezing rain is diagnosed to be present if rain reaches a subfreezing land surface. Ice pellets are simply diagnosed in the present case by the mutual satisfaction of (i) the presence of an AFIL overlying a surface subfreezing layer and (ii) the presence of ice/snow at the surface. When compared to the observed sequence of precipitation change over the region (Fig. 3), the snow ends too quickly in the simulation, the onset of ice pellets is quite well predicted but it lasts too long, the onset of freezing rain is too early and also lasts too long, and the onset of rain is slightly too late in the model. When comparing Fig. 10 against Figs. 9g and 9h, it is apparent that the maximum precipitation rates are associated with ice pellets and rain, whereas the minimum rates are associated with freezing rain; both of these storm characteristics agree with the observations (Fig. 3).

The main discrepancies between the observed and simulated surface precipitation types are caused by (i) the use of instantaneous melting and (ii) the use of a single ice variable in the model. Considering that ice pellets are rarely observed when the depth of the surface subfreezing layer is less than about 800 m (Stewart and Crawford 1995), the present cloud scheme seems to be overpredicting the rates of raindrop refreezing in regions of $y < 150$ km (see Figs. 9a and 9g,h). On the other hand, the temperatures within 40 km of the tip of the AFIL are <2°C. As such, the snow particles falling into this region will mainly only be partially melted and they can refreeze to form ice pellets quite quickly in the deep surface subfreezing layer beneath it. Therefore, the use of a more sophisticated microphysical package (e.g., one that carries variables for different ice categories and calculates the melting term explicitly) in the simulation would most likely delay the onset of freezing precipi-

tation while reducing the extent of the ice pellets region to values in better agreement with observations.

In summary, some details of the observed storm structure (e.g., its thermal and kinematic structure) and some aspects of the observed precipitation field (such as the locations of the precipitation bands and, to a lesser degree, their intensity and associated surface precipitation types) have been quite well replicated in the simulation. As such, the dynamic processes in the model storm should also reflect some degree of reality and an examination of these processes by using the model results should enhance our physical understanding of these types of storms.

5. Diagnosis and discussions of model results

The physical processes responsible for the development of a freezing rain episode in the model results will be analyzed in this section. In particular, the precipitation band generating mechanisms, the diabatic effects of the precipitation processes and mechanisms that affect the development of the AFIL, will be discussed. Since the thermal and kinematic structure of the warm-frontal zone is quasi-two-dimensional (apart from the surface layer where the influences of the surface features over the peninsula are apparent) over the region of interest (Fig. 7a), the 2D assumption is used in some of the arguments where appropriate. A conceptual model summarizing the model results and the identified physical processes that are important to the development of the system will then be presented at the end of this section.

a. The generation of precipitation bands

Various mechanisms have been proposed to explain the formation of banded precipitation features in extratropical cyclones [see, e.g., Parsons and Hobbs (1983) for a brief review of these mechanisms]. The three bands of precipitation developed in both the observed and the simulated storms have characteristics (their orientation, width, separation distances, and intensity) that are typical of wide warm-frontal precipitation bands (e.g., see Houze and Hobbs 1982). Conditional symmetric instability (CSI; Bennets and Hoskins 1979) has been a particularly attractive theory for explaining the generation of wide warm-frontal precipitation bands since it accounts for many of the important mesoscale characteristics of the bands such as their horizontal scale and orientation. In the 2D linear theory, the inviscid criterion for instability in a saturated two-dimensional baroclinic flow in the Northern Hemisphere is that the moist potential vorticity (MPV $\equiv \boldsymbol{\omega}_a \cdot \nabla\theta_e/\rho$, where $\boldsymbol{\omega}_a$ is absolute vorticity and ρ is air density) be negative. While a thorough assessment of CSI in the model results (see, e.g., Persson and Warner 1995) is outside the scope of this paper, a preliminary assessment is performed by examining the MPV field of the model storm at 1800 UTC 26 February and 0000 UTC 27 February along AA′ (Figs. 11a and 12a).

At 1800 UTC 26 February, an extensive and deep area of weakly negative MPV was found at regions above the warm-frontal zone (Fig. 11a). The air within this region above the frontal zone is therefore symmetrically unstable for saturated motions according to the MPV < 0 criterion. The $\partial\theta_e/\partial z$ field (Fig. 11b) shows that a significant portion of this negative MPV region is also near neutral or weakly unstable to saturated vertical ascent (i.e., $\partial\theta_e/\partial z \leq 0$), suggesting that the part of the warm sector air mass has gone through convective adjustment at lower latitudes. A thin but quite strong negative MPV layer is also found near the weak updraft cores located along and just above the sloping low-level frontal zone (Figs. 8d and 11a). In fact, the separation distance of the two updraft cores ($\sim$75 km) is also in agreement with the prediction of CSI theory (i.e., $L \sim HU_z/f$ in stably stratified conditions, where L is horizontal length scale of the overturning rolls, H is the depth of the unstable layer which is about 1 km in this case, f is the Coriolis parameter, and $U_z \sim 7.5$ s^{-1} is the mean vertical shear within the layer; see Figs. 8e,f). Although these circulation cells are too weak and too shallow to have significant effects on the distribution of precipitation, they affect the local frontal topography, as is evident in Figs. 8c and 9c (see also Locatelli et al. 1994).

By 0000 UTC 27 February, an extensive and organized layer of negative MPV is found to be located roughly between 2 and 4 km above ground level (AGL) (Fig. 12a). It is noteworthy that the updraft cores associated with all three bands (see Figs. 9d and 9h) are located within this layer of air characterized by negative MPV (although not visible in Fig. 12a, the midlevel negative MPV layer extends farther north and encompass the updraft core of band B1). Similar to the conditions at 1800 UTC 26 February, a substantial portion of the air in the midlevel negative MPV layer is also near neutral or weakly unstable to saturated ascent (Fig. 12b). In particular, the midlevel updraft core (W3) associated with band B3 is embedded in a region of potential instability (Fig. 12b), suggesting that band B3 was a result of weak convective instability. Weak convective activity within the corresponding third band (B3 in Fig. 2b) was also evident in the observations (see section 2 and HSTL). On the other hand, the updraft cores associated with bands B2 and B1 are embedded within a weakly stably stratified region (see Figs. 9d and 12b), and CSI is a probable candidate responsible for their formation. Patchy regions of negative MPV are also found within the sloping frontal zone (between 0.5 and 2 km AGL in Fig. 12a) but they are not as organized and not as strong as the negative MPV that are observed in that region at 1800 UTC 26 February (Fig. 11a).

Recent studies (e.g., Persson and Warner 1991) have shown that numerical artifacts, such as spurious gravity waves, which can contaminate the resolved features,

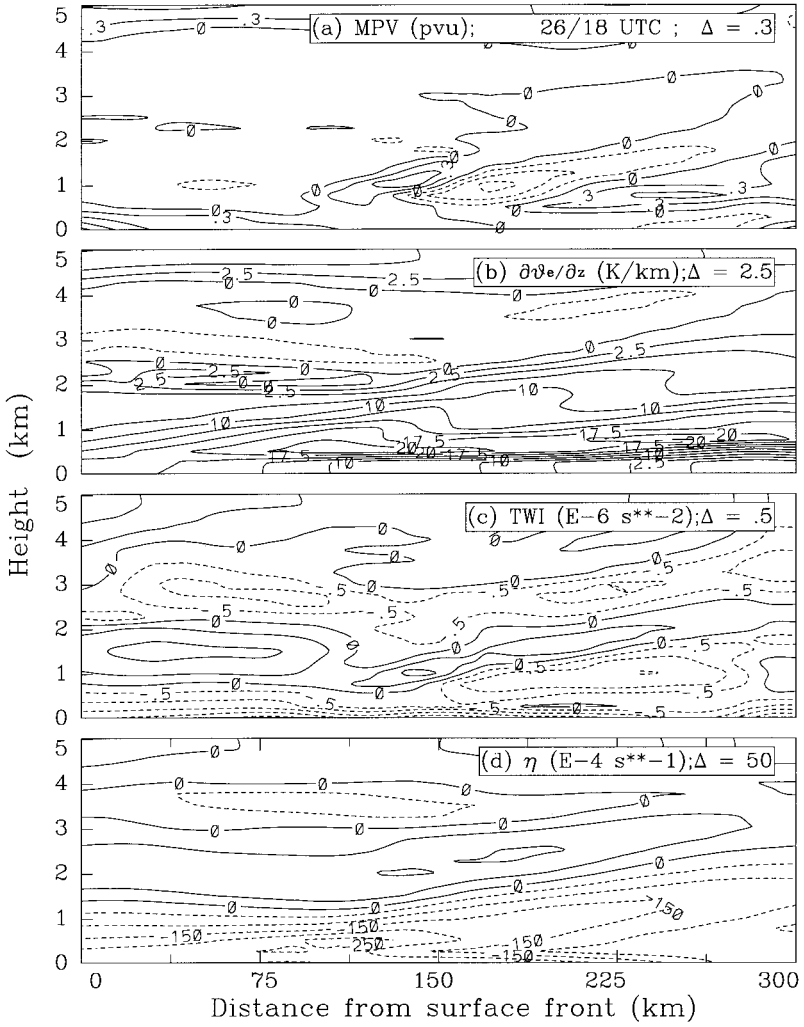

FIG. 11. Cross sections of various fields along line AA′ at 1800 UTC 26 February from the BULKMIC10 simulation: (a) moist potential vorticity, (b) θ_e lapse rate, (c) thermal wind imbalance, and (d) alongfront vorticity.

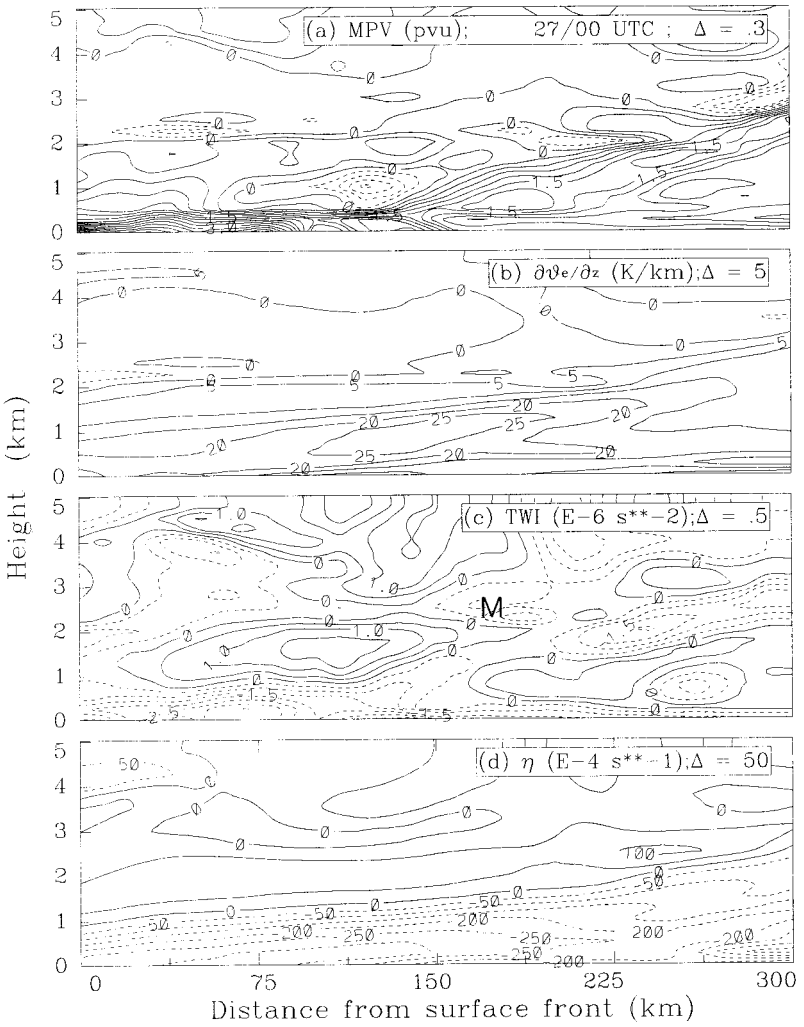

FIG. 12. As in Fig. 11 but at 0000 UTC 27 February.

might be induced if inappropriate model resolutions were employed (i.e., the ratio of the vertical resolution to the horizontal resolution should be equal to or less than the slope of the main features of interests in the simulation, e.g., the frontal zone in this case). A simulation performed with the vertical resolution increased to 75 m at the lower levels (so that the ratio of the vertical and horizontal resolutions is approximately equal to the observed warm frontal zone) shows no significant differences in the structures and in the development of negative MPV regions in the model storm, showing that the banded features developed in the current simulations are not artifacts induced by inconsistent model resolution. It should also be noted that the discussions given above are based on the results of idealized 2D theories of CSI (e.g., Bennetts and Hoskins 1979) that may not be applicable to the present situation. For example, Bennetts and Hoskins (1979), Xu (1986), and Persson and Warner (1993) showed that a more stringent instability criterion than MPV < 0 must be used for viscous CSI or CSI with a finite updraft width (e.g., such as in a numerical model or in reality). In addition, the presence of frontal forcing, microphysical effects, and topographic influences can further complicate the diagnosis of precipitation formation mechanisms in the model results. As such, although the preliminary analysis presented here suggests CSI as a probable generating mechanism for some of the precipitation bands in the model storm, much more thorough analyses than presented here are required for a rigorous assessment of CSI in the model storm.

b. Precipitation-induced diabatic effects

The precipitation particles changed phase as they fell through AFIL. Since the region ahead of the surface warm front is characterized by a deep and extensive saturated layer, there is no evidence of rain evaporation at lower levels in both the model results and in the observed system. In addition, the sublimation of snow below cloud is only significant at regions quite remote from the surface front (at distances >350 km ahead of the front at 0000 UTC 27 February). Therefore, the main precipitation-induced diabatic processes are the melting of snow to form rain at the melting layer and the refreezing of rain to the ice phase below the AFIL. Due to the high terminal velocities of raindrops (~ 5 m s^{-1}), the refreezing of rain to the ice phase typically occurs over a deep distance (see Figs. 9g,h). In addition, the refreezing process requires abundant ice nuclei at the low levels if the snowflakes have completely melted within the inversion (or an ice embryo embedded within partially melted particles). On the other hand, the melting of snow to form rain is typically completed within a layer of a few hundred meters due to the slow fall speeds of snowflakes (~ 1 m s^{-1}). As such, quite strong cooling rates can be induced by the melting process. The heating rates associated with refreezing in the lower levels are typically one-quarter to one-third of those associated with melting snow (see Fig. 14).

Recent studies (Szeto et al. 1988a,b; Stewart et al. 1996; Szeto and Stewart 1997b) show that the effects of melting are most appreciable when it occurs in a baroclinic environment, such as in the vicinity of a frontal zone. In particular, horizontally differential cooling by melting occurs (even when the precipitation rate is stratiform) when the 0°C isotherm is sloping downward to the cold side of a baroclinic environment, for example, near the nose of the AFIL. Horizontally different cooling by melting can also occur in a barotropic environment when there are horizontal variations in the precipitation rate. The differential cooling enhances (and decreases) the local baroclinicity and modulates the circulation at the location. When the alongfront variations in precipitation rate and temperature are neglected, the dynamical effects of the cooling by melting mechanism can be examined by using the alongfront vorticity equation

$$\frac{D\eta}{Dt} = \left(\frac{\partial B}{\partial y} + f\frac{\partial u}{\partial z}\right) + F_\eta, \tag{1}$$

where $\eta \equiv (\partial w/\partial y - \partial v/\partial z)$ is the vorticity component in the alongfront direction, B is total buoyancy, u is the alongfront wind, and F_η represents subgrid effects. The term in parentheses will be called thermal wind imbalance (TWI) (Orlanski and Ross 1977; Redelsperger et al. 1994), which gives a measure of the departure of the local environment from thermal wind balance. The neglected terms in Eq. (1) (i.e., terms involving the alongfront derivatives of the various wind components) are largest in the boundary layer, but even there the maximum and typical magnitude of these terms are an order of magnitude smaller than the TWI values in the region. Therefore, the use of Eq. (1) is justified in the following semiqualitative discussions. When the melting of snow produces a horizontal variation in buoyancy, it creates TWI since the adjustment of the atmosphere back to the quasigeostrophic state is a much slower process than the melting process, thereby inducing a local circulation via Eq. (1) (Szeto et al. 1988a).

The enhancement of frontal contrast by differential cooling by melting near the nose of the AFIL is evident in the model results (see Fig. 9b at y near 180 km and $z \sim 2$ km) and in the observations (see Fig. 8 of HSTL). The TWI field at 1800 UTC 26 February and 0000 UTC 27 February across the line AA′ is calculated from the model results and presented in Figs. 11c and 12c, respectively. A negative TWI anomaly can be found at the melting-induced enhanced baroclinic region (marked ''M'' in Fig. 12c at $y \sim 180$ km and ~ 2 km AGL). Depending on the background conditions, various configurations of flow perturbation can be induced by these melting-induced cooling effects (Szeto et al. 1988a,b). In particular, when a mean flow is present in the melting layer (such as in the present case at 0000

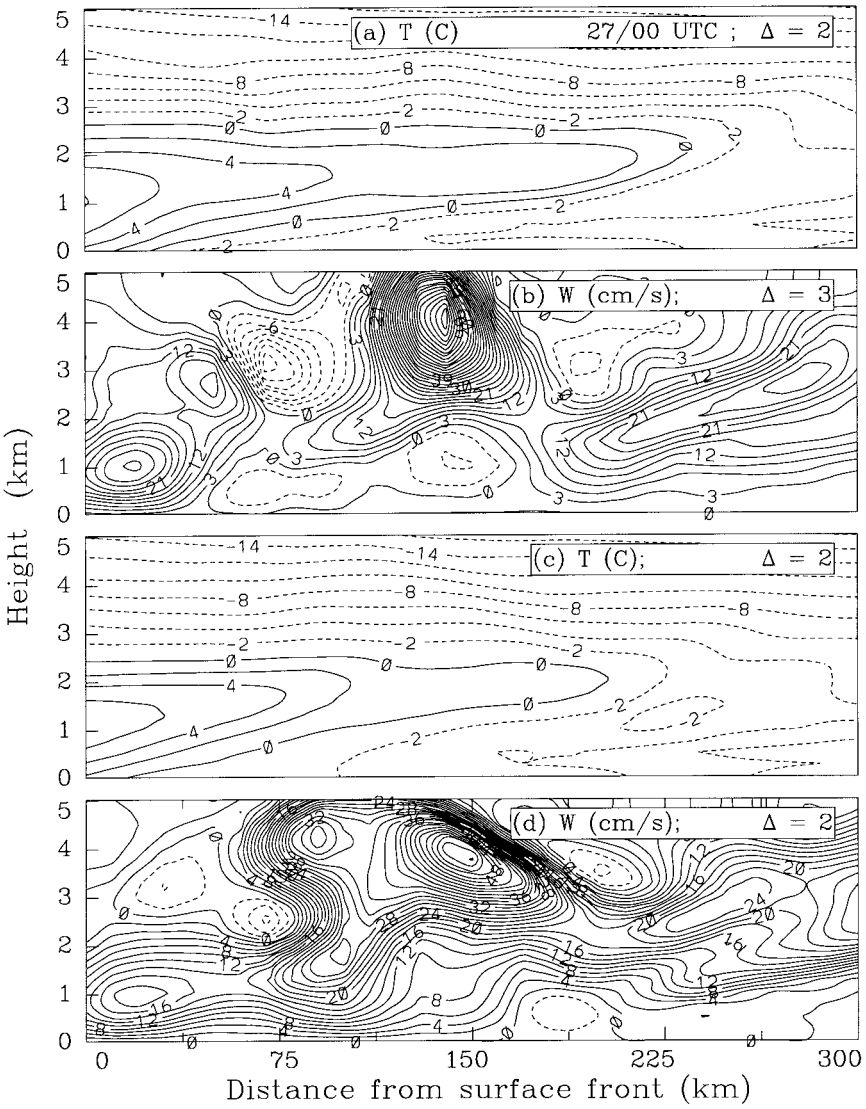

FIG. 13. Cross sections of temperatures and vertical velocities along line AA′ at 0000 UTC 27 February from experiments WARM_RAIN [(a) and (b)] and NO_TOPO [(c) and (d)].

UTC 27 February), an updraft is induced in the immediate upwind location of the region affected by maximum cooling (Szeto et al. 1988a).

When the air above the melting level is either potentially or symmetrically unstable, interesting coupling effects between convective cells–CSI rolls and cooling by melting can occur. First, an updraft is induced when the cross-front flow encounters the enhanced baroclinic region induced by the differential cooling by melting (see the local enhancement of *w* near the melting-induced perturbation on the frontal surface in Figs. 9c and 9d). This updraft might act as a finite-amplitude triggering mechanism for the release of CSI above the melting level in marginal cases. Later, this updraft could reinforce that of the CSI roll located above the melting level and enhance the precipitation production, which will in turn maintain or further enhance the differential cooling by melting, and so on. The result is an enhanced precipitation band located beneath the nose of AFIL as is evident in the model results and in the observations. Such strong coupling effects between cooling by melting and weak convective cells are also evident in the 2D simulation results of Szeto and Stewart (1997b) (see their Figs. 12 and 13).

Depending on the depth and temperatures of the surface subfreezing layer, the melted snow in the AFIL might refreeze to form either ice pellets (when the refreeze is completed aloft) or freezing rain (when the refreeze occurs at the surface). One might therefore infer from the above discussions that enhanced surface precipitation rates (i.e., banded precipitation features) are likely to accompany the passage of surface precipitation

type transition regions (PTTRs) in winter storms. Such an inference is supported by the observational study of PTTRs carried out by Stewart et al. (1995). For example, enhanced precipitation rates were found within the PTTR in 9 out of the 11 CASP II storms that possessed a PTTR. One might further infer that the most hazardous situation would occur when the height of the upper 0°C isotherm is low (say, $<$1.5 km AGL), when the heaviest precipitation would then be associated with freezing rain rather than with the less ''harmful'' ice pellets such as in the present case.

The bulk effects of ice phase processes on the system can be examined by comparing the results from experiments BULKMIC10 and WARM_RAIN. Figures 13a,b show the temperature and vertical velocities along AA′ for the WARM_RAIN run at 0000 UTC 27 February. While the overall thermal structure of the model storm is similar to that in case BULKMIC10 (Fig. 9a), the strong updraft core corresponding to W2 in case BULKMIC10 is now occurring much closer to the surface front (see Figs. 13b and 9d), in support of the arguments given above. It should also be noted that the strongest precipitation in this case would have been diagnosed to be associated with freezing rain rather than ice pellets (as in case BULKMIC10) due to the increased depth of the AFIL and the decreased depth of the surface subfreezing layer beneath the second band in this case. Therefore the inclusion of ice phase processes in the model is important for the accurate prediction of band locations and precipitation types in this kind of storm.

c. The AFIL

The temperature, depth, and extent of the AFIL are all critical factors that determine the final form of precipitation that reaches the surface in the model storm. The processes that affect the evolution and structure of the AFIL in the model storm will be discussed in this section.

The development of frontal inversions is mainly a consequence of the conversion of the available potential energy to kinetic energy in baroclinic disturbances and, therefore, depends largely on the baroclinicity of the background flow and frontal-scale dynamics. On the frontal scale, such inversion layers are mainly the result of differential temperature advection in the vertical (i.e., warm advection aloft and cold advection at the lower levels) by the cross-front shear flow. As such, the vertical shear of the cross-front flow at the low levels plays an important role in the development of the AFIL.

Insights into the evolution of the vertical shear of the cross-front flow can also be obtained from the along-front vorticity equation [Eq. (1)] along with the following approximation for η at the low levels:

$$\eta \equiv (\partial w/\partial y - \partial v/\partial z) \approx -\partial v/\partial z. \qquad (2)$$

Since $\partial v/\partial z$ is typically two orders of magnitude larger than $\partial w/\partial y$ at or below the frontal zone, (2) is a good approximation for η in the region of interest. Therefore, if the subgrid-scale eddy effects are neglected, Eqs. (1) and (2) would imply that the evolution of the vertical shear of the cross-front wind is governed by the production of TWI in the region.

Thermal wind imbalance can result from several different processes such as frontal collapse, surface friction, and diabatic processes associated with clouds and precipitation (see Redelsperger et al. 1994, as well as the discussion in section 5b). From Figs. 11c and 12c, the strongest TWI values are found in the boundary layer at both model times due to the deceleration of the alongfront flow by surface drag and therefore the imbalance between the rotation term ($f\partial u/\partial z$) and the solenoidal term ($\partial B/\partial y$) inside the planetary boundary layer (PBL). This effect is particularly strong when the system reaches the Avalon peninsula (i.e., near 0000 UTC 27 February; see Fig. 12c), where the effective surface drag (due to the changes in surface roughness and the topographic features over the island) increased markedly when compared to when the system was over the ocean (Fig. 11c). The effect of negative TWI in the PBL was the production of negative η (i.e., positive vertical cross-front shear) and enhancements of the cross-front ageostrophic circulation over the region (Figs. 11d and 12d). An indirect effect of the TWI generation inside the PBL is the accelerated frontogenesis induced by the enhanced ageostrophic cross-front circulation near the surface front. Another consequence of the enhanced ageostrophic low-level cross-front circulation is the ''flattening'' of the frontal zone just ahead (to the cold side) of the surface front (see Fig. 9b near 120 km).

Results from the no topography (NO_TOPO) simulation are given in Figs. 13c,d. Effects of topography on the development of the AFIL are clearly demonstrated in these results: the width and depth of the AFIL are significantly narrower and shallower and the temperatures within the AFIL are significantly lower than those in the BULKMIC10 case. The strength of the surface front is also somewhat weaker in this case. It is of interest to note that the strongest updraft core in this case is also located near the nose of the AFIL (Figs. 13c,d) where the melting effects are most significant, in agreement with the predictions of the arguments given in section 5b.

Other processes can also be identified to contribute to the TWI distribution depicted in Fig. 12c. For example, the midlevel subsidence induced by the convective band B3 induces low-level divergence when it encounters the highly stable low-level frontal zone. This local ageostrophic divergent flow induces a broad positive TWI anomaly above the PBL just ahead of the surface front. This positive TWI anomaly combines with strong negative TWI anomaly within the PBL to produce a strong cross-front jet located just above the PBL (Fig. 9e), which promotes strong warm temperature advection above the PBL.

While the ageostrophic cross-front circulation promotes the development of the inversion layer, the temperatures within and below the layer are determined by the thermal characteristics of the warm sector air mass and the temperatures at low levels ahead of the surface front. Due to the warm water current off the east coast of North America, the winter maritime air mass is typically quite warm and moist with the 0°C level located near ~2.5 km altitude. On the other hand, the near-surface temperatures over Newfoundland are substantially below freezing during the winter months (there is extensive sea ice coverage off the northern and east coasts of Newfoundland, see Fig. 1). Consequently, broad AFILs such as the one depicted in Fig. 9a are typical over the region during the passage of winter storms due to the combined effects of frontal dynamics, surface layer processes, and the characteristics of the winter air mass over the Maritimes.

While many processes lead to the development of AFILs, there are also processes that act to destroy the AFILs. These processes include (i) adiabatic cooling or heating associated with vertical motions and (ii) latent cooling or heating associated with the phase change of water substance. Since the whole storm cross section along AA′ is near or at saturation, effects of evaporation and sublimation processes are minimal in the region of interest here. If we also neglect the radiative diabatic effects and diffusional effects, the local change of temperature is govened by

$$\frac{\partial T}{\partial t} = -u\frac{\partial T}{\partial x} - v\frac{\partial T}{\partial y} - w\left(\frac{\partial T}{\partial z} + \Gamma_d\right) + (C + M + F), \quad (3)$$

where Γ_d is the adiabatic lapse rate (~10 K km^{-1}) and C, M, F represent the heating rates due to condensation–deposition, melting, and freezing (with effects of riming and accretion also included in this term just for the sake of simplicity), respectively. The instantaneous heating budgets at the low levels at $y \sim 200$ km are presented in Fig. 14. At $y \sim 200$ km where the precipitation is strongest in the model storm along AA′ at 0000 UTC 27 February, the maximum melting-induced cooling rate is about 8.5 K h^{-1} and concentrated within a layer of about 500 m centered at 2 km AGL. The heating rates induced by the refreezing have magnitudes between ~2 and 3 K h^{-1} and are limited essentially to the lowest 1.5 km. It is also of interest to note the enhanced condensational heating near the top of the melting layer where the cooling by melting induced supersaturation condition in the region. At this location, horizontal temperature advection is closely balanced by adiabatic cooling associated with the updraft at the low levels. The net local change of temperature is therefore determined largely by microphysical effects and tends to limit the development of the AFIL (i.e., cooling the upper region of the AFIL while warming its lower region). For example, a lowering of the melting level toward the ''nose'' of the AFIL is noticeable in Figs. 9a and 9h but not in Fig. 13a. However, it should be noted that the precipitation-induced diabatic effects decrease rapidly away from the precipitation core and the effects of temperature advection become more important in determining the thermal structure at regions closer to the surface front.

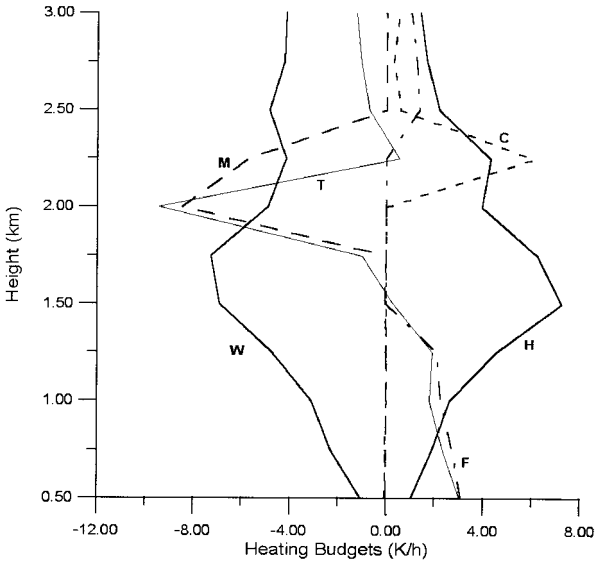

FIG. 14. Profiles of heating budgets at $y = 200$ km with H denoting the horizontal advection, W denoting vertical advection and adiabatic cooling, C denoting condensation heating, M denoting melting, F denoting freezing, and T denoting the net heating rate.

d. Conceptual model

Based on the model results and the discussions of the physical processes that occurred in the model storm, a conceptual model that summarizes the main features of the 26 February freezing rain storm in the vicinity of the warm front and the processes that are responsible for the development of these feature is developed (Fig. 15). By the time the surface warm front approached the Avalon peninsula, an extensive region above the frontal zone was characterized by either $\partial\theta_e/\partial z \leq 0$ or weakly negative MPV, suggesting the region was either potentially or symmetrically unstable to saturated motions (regions denoted by CI or CSI in Fig. 15). Saturated conditions throughout a deep region ahead of the surface front were created by moisture fluxes from the ocean surface and weak surface layer rising motions in the cold sector adjacent to the surface front. Stable ascent within and above the frontal zone produced extensive cloud and light precipitation ahead of the surface front.

The system was undergoing a period of enhanced warm frontogenesis by the time the surface front reached the peninsula. The step change in surface characteristics (surface roughness and topography) perturbed the alongfront jet (J1) away from a state of (qua-

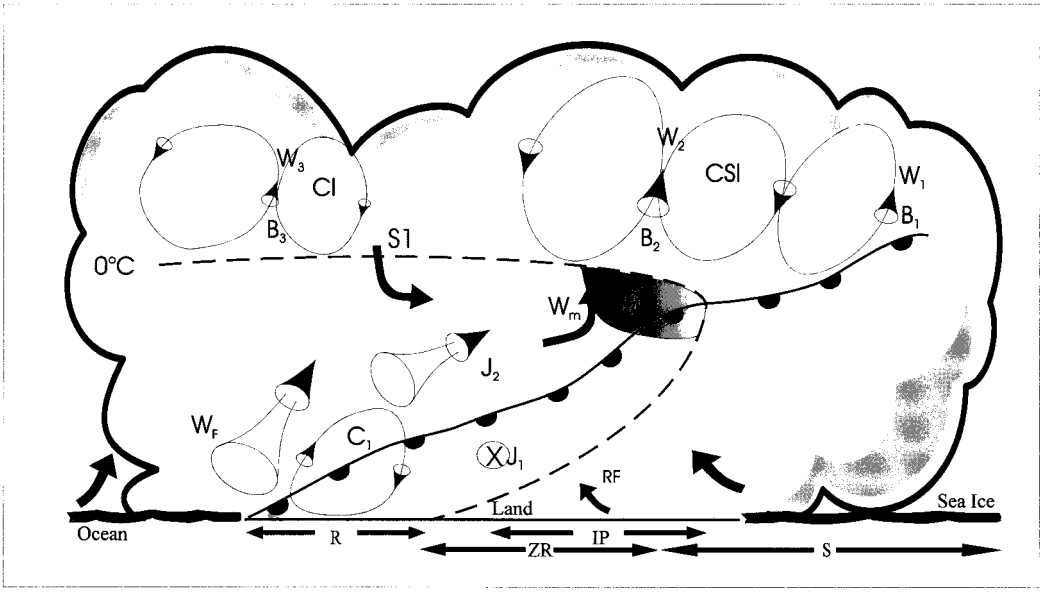

FIG. 15. A conceptual model of the 26 February storm as deduced from model results. The letters denote storm features and processes that are detailed in section 5d.

si-) thermal wind balance with the cross-front temperature gradients. The thermal wind imbalance intensified the cross-front ageostrophic circulation (C1), which enhanced surface frontal convergence, strengthened the frontal uplift (W_F), and accelerated surface frontogenesis. Circulation C1 also enhanced the vertical cross-front shear in the PBL, which in turn intensified the differential temperature advection in the vertical and led to the formation of a deep and extensive above-freezing inversion layer at the low levels. Shallow circulations (not shown) that developed along the frontal surface are possibly symmetric rolls that developed when CSI was released inside the shallow zone of negative MPV air there. Flow perturbations associated with these rolls were not strong or deep enough to have significant effects on the precipitation field, but they were strong enough to modulate the local topography and thermal contrast of the frontal zone.

Weak convective motion created main updraft W3, which in turn generated precipitation band B3 near the surface front. Deep mesoscale circulations, possibly associated with CSI at the midlevels, created main updrafts W2 and W1, which produced precipitation bands B2 and B1 at roughly 200 and 320 km from the surface front. The circulation associated with B3 interacted with that associated with B2 to produce subsidence (S1) at midlevels. The subsidence in turn interacted with circulation C1 to produce the low-level cross-front jet core J2.

The snow generated in band B3 melted to form rain at the surface, while the precipitation from band B1 reached the surface in the form of snow due to the predominant subfreezing temperatures in that region. A large portion of the snow generated from band B2 melted when it fell into the AFIL. Part of the melted snow refroze at low levels (regions denoted by RF in Fig. 15) to form ice pellets (IP) while part of it refroze only on impact with the subfreezing surface to form freezing rain (ZR). The melting of snow near the nose of the AFIL created an enhanced local baroclinic zone (M) and perturbed the cross-front flow in the region. The updraft (Wm) associated with this melting-induced flow perturbation might have triggered the formation of the symmetric roll associated with band B2; later it interacted with updraft W2 through a positive feedback process to produce the strong precipitation band B2.

The conceptual model depicted in Fig. 15 compares quite well with the one developed by HSTL based on observations. In particular, the double jet structure, the location of the precipitation bands, the distribution of surface precipitation types, and the structure of the perturbed frontal surface are similar in both conceptual models, suggesting that the mesoscale structure of the system had been quite successfully replicated in the model. Analysis of the model results allowed the extension of the conceptual model of HSTL by identifying the physical processes responsible for the development of the mesoscale storm features.

6. Concluding remarks

A severe freezing rain–producing winter storm affected the east coast of Canada on 26 February 1992 that was observed with a number of special measurements during the CASP II field project. A hierarchy of cloud-resolving model simulations of this storm was performed with the objective of enhancing our understanding of the physical nature of freezing rain storms

over the region. The overall features of the system were quite well replicated in the high-resolution simulation. An analysis of the model results has led to a number of conclusions.

1) The change of surface characteristics from ocean to land in the vicinity of the surface warm front accelerates warm frontogenesis and intensifies the cross-frontal circulation, which in turn leads to the development of an extensive above-freezing inversion layer in the model storm. Cooling by melting below the 0°C level and warming of the lowest levels by the refreezing of rain tend to limit the development of the above-freezing inversion layer in the mature storm.
2) The phase change of precipitation within the inversion layer and the evolution of surface precipitation types in winter storms can be reasonably well simulated by cloud models that include a bulk water–type cloud scheme carrying independent variables for the different phases of water substance. In particular, the model results suggest that the inclusion of ice pellets and the use of explicit melting rate calculations in the model might improve the prediction of surface precipitation types in such storms.
3) Potential instability and conditional symmetric instability are probable mechanisms that were responsible for the various banded precipitation features in the model storm. However, the real-life conditions complicate the assessment of these processes in the model storm and a deeper analysis of the model results than those carried out in this preliminary study are needed before more conclusive statements can be given on this aspect of the storm.
4) Model results suggest that perturbations induced by the cooling effects of melting snow on the cross-front flow near the nose of the above-freezing inversion layer might trigger the formation of symmetric or convective overturning above the region and consequently enhance the local precipitation production via a positive feedback mechanism. Therefore, depending on the height of the melting level, enhanced precipitation rates are likely to accompany the occurrence of ice pellets or freezing rain at the surface.
5) The local frontal topography and local baroclinicity of the frontal zone can be significantly affected by ageostrophic circulations induced by surface effects and cooling by melting near the nose of the above-freezing inversion layer.
6) The overall mesoscale structure of winter storms can be reasonably well simulated by models using horizontal resolutions (~25 km) and cloud schemes similar to those used in current state-of-the-art forecast models. However, the finer-scale structures of the storms that can critically affect the accurate forecasting of the onset, the duration, and the intensity of freezing rain episodes are not satisfactorily resolved in such simulations.
7) Predictions of both the evolution and finescale storm structures of winter storms can be substantially improved in models that employ horizontal resolutions less than 10 km and include a reasonably sophisticated explicit cloud scheme. Advances in supercomputer technology are approaching the level that makes real-time simulation of these storms with high-resolution cloud models a practical and feasible task. Therefore, the prospect for reliable dynamic nowcasting of severe and hazardous winter storm events is promising.

Acknowledgments. The authors wish to thank the three anonymous reviewers for the insightful comments that have considerably improved the manuscript. The authors also wish to thank Mr. Jim Young for assistance in the preparation of the manuscript. This research was supported in part by the Federal Panel on Energy Research and Development (PERD).

REFERENCES

Barth, M. C., and D. B. Parsons, 1996: Microphysical processes associated with intense frontal rainbands and the effects of evaporation and melting on frontal dynamics. *J. Atmos. Sci.,* **53,** 1569–1586.

Bennetts, D. A., and B. J. Hoskins, 1979: Conditional symmetric instability—A possible explanation for frontal rainbands. *Quart. J. Roy. Meteor. Soc.,* **105,** 945–962.

Benoit, R., J. Cote, and J. Mailhot, 1989: Inclusion of TKE boundary layer parameterization in the Canadian regional finite-element model. *Mon. Wea. Rev.,* **117,** 1726–1750.

——, M. Desgagne, P. Pellerin, S. Pellerin, and Y. Chartier, 1997: The Canadian MC2: A semi-Lagrangian, semi-implicit wideband atmospheric model suited for finescale process studies and simulation. *Mon. Wea. Rev.,* **125,** 2382–2415.

Bocchieri, J. R., 1980: The objective use of upper air soundings to specify precipitation type. *Mon. Wea. Rev.,* **108,** 596–603.

Chang, S. A., R. J. Alliss, S. Raman, and J.-J. Shi, 1993: SSM/I observations of ERICA IOP 4 marine cyclone: A comparison with in situ observations and model simulation. *Mon. Wea. Rev.,* **121,** 2452–2464.

Crawford, R. W., and R. E. Stewart, 1995: Precipitation types characteristics at the surface in winter storms. *Cold Reg. Sci. Technol.,* **23,** 215–229.

Donaldson, N. R., and R. E. Stewart, 1993: On the influence of trajectories on precipitation type characteristics in winter storms. *Contrib. Atmos. Physics,* **66,** 2125–2136.

Erickson, M. C., J. P. Dallavalle, and J. S. Jensenius Jr., 1993: Comments on ''Snow versus rain: Looking beyond the 'magic' numbers.'' *Wea. Forecasting,* **8,** 542–544.

Gedzelman, S. D., and R. Arnold, 1993: The form of cyclonic precipitation and its thermal impact. *Mon. Wea. Rev.,* **121,** 1957–1978.

Hanesiak, J. M., and R. E. Stewart, 1995: The mesoscale and microscale structure of a severe ice pellet storm. *Mon. Wea. Rev.,* **123,** 3144–3162.

Heppner, P. O. G., 1992: Snow versus rain: Looking beyond the magic numbers. *Wea. Forecasting,* **7,** 683–691.

Houze, R. A., Jr., and P. V. Hobbs, 1982: Organization and structures of precipitating cloud systems. *Advances in Geophysics,* Vol. 24, Academic Press, 225–315.

Hudak, D. R., R. E. Stewart, A. D. Thomson, and R. List, 1996:

Warm frontal structure in association with a rapidly deepening extratropical cyclone. *Atmos.–Ocean,* **34,** 103–132.
Huschke, R. E., 1959: *Glossary of Meteorology*. Amer. Meteor. Soc., 638 pp.
Knight, P. G., 1996: Ice storms. *Encyclopedia of Climate and Weather.* Vol. 1, Oxford University Press.
Kong, F.-Y., and M. K. Yau, 1997: An explicit approach of microphysics in MC2. *Atmos.–Ocean,* **35,** 257–291.
Kuo, H. L., 1974: Further studies of the parameterization of the influence of cumulus convection on large-scale flow. *J. Atmos. Sci.,* **31,** 1232–1240.
Kuo, Y. H., M. A. Shapiro, and E. G. Donall, 1991: The interaction between baroclinic and diabatic processes in a numerical simulation of a rapidly intensifying extratropical marine cyclone. *Mon. Wea. Rev.,* **119,** 368–384.
Lamb, H. H., 1955: Two-way relationship between the snow and ice limits and 1000–500 mb thickness in the overlaying atmosphere. *Quart. J. Roy. Meteor. Soc.,* **81,** 172–189.
Locatelli, J. D., J. E. Martin, and P. V. Hobbs, 1994: A wide cold-frontal rainband and its relationship to frontal topography. *Quart. J. Roy. Meteor. Soc.,* **120,** 259–275.
Orlanski, I., and B. B. Ross, 1977: The circulation associated with a cold front. Part I: Dry case. *J. Atmos. Sci.,* **34,** 1619–1633.
Parsons, D., and P. V. Hobbs, 1983: The mesoscale and microscale structure and organization of clouds and precipitation in midlatitude cyclones. Part XI: Comparisons between observational and theoretical aspects of rainbands. *J. Atmos. Sci.,* **40,** 2377–2397.
Persson, P., and G. Ola, 1993: Sensitivity studies of nonlinear hydrostatic conditional symmetric instability: Implications for numerical weather prediction. *Mon. Wea. Rev.,* **121,** 1821–1833.
——, and ——, 1995: The nonlinear evolution of idealized, unforced, conditional symmetric instability: A numerical study. *J. Atmos. Sci.,* **52,** 3449–3474.
——, ——, and T. T. Warner, 1991: Model generation of spurious gravity waves due to the inconsistency of the vertical and horizontal resolution. *Mon. Wea. Rev.,* **119,** 917–935.
Pike, W. S., 1995: Extreme warm frontal icing on 25 February 1994 causes an aircraft accident near Uttoxeter. *Meteor. Appl.,* **2,** 273–279.
Redelsperger, J.-L., J. P. Lafore, C. Cailly, and E. Arbogast, 1994: Nonhydrostatic simulations of frontogenesis in a moist atmosphere. Part III: Thermal wind imbalance and rainbands. *J. Atmos. Sci.,* **51,** 3467–3485.
Stewart, R. E., 1991: Canadian Atlantic Storms Program: Progress and plans of the meteorological component. *Bull. Amer. Meteor. Soc.,* **72,** 364–371.
——, 1992: Precipitation types in the transition region of winter storms. *Bull. Amer. Meteor. Soc.,* **73,** 287–296.
——, and R. W. Crawford, 1995: Some characteristics of the precipitation formed within winter storms over eastern Newfoundland. *Atmos. Res.,* **36,** 17–37.
——, D. T. Yiu, K. K. Chung, D. R. Hudak, E. P. Lozowski, M. Oleskiw, B. E. Sheppard, and K. K. Szeto, 1995: Weather conditions associated with the passage of precipitation type transition regions over eastern Newfoundland. *Atmos.–Ocean.,* **33,** 25–53.
——, R. W. Crawford, K. K. Szeto, and D. R. Hudak, 1996: Horizontal aircraft passes across 0°C regions within winter storms. *Atmos.–Ocean,* **34,** 133–159.
Sundqvist, H., E. Berge, and J. E. Kristjansson, 1989: Condensation and cloud parameterization studies with a mesoscale numerical weather prediction model. *Mon. Wea. Rev.,* **117,** 1641–1657.
Szeto, K. K., and R. E. Stewart, 1997a: Cloud model simulations of surface weather conditions associated with the warm-frontal regions of winter storms. *Atmos. Res.,* **44,** 243–269.
——, and ——, 1997b: The effects of melting on frontogenesis. *J. Atmos. Sci.,* **54,** 689–702.
——, C. A. Lin, and R. E. Stewart, 1988a: Mesoscale circulations forced by melting snow. Part I: Basic simulations and dynamics. *J. Atmos. Sci.,* **45,** 1629–1641.
——, R. E. Stewart, and C. A. Lin, 1988b: Mesoscale circulations forced by melting snow. Part II: Application to meteorological features. *J. Atmos. Sci.,* **45,** 1642–1650.
Tanguay, M. A., A. Robert, and R. Laprise, 1990: A semi-implicit semi-Lagrangian fully compressible regional forecast model. *Mon. Wea. Rev.,* **118,** 1970–1980.
Taylor, P. A., J. R. Salmon, and R. E. Stewart, 1993: Mesoscale observations of surface fronts and low pressure centres in Canadian East Coast storms. *Bound.-Layer Meteor.,* **64,** 15–54.
Tremblay, A., 1994: Simulations of the 15 July 1987 squall line using a fully compressible model. *Atmos.–Ocean,* **32,** 567–603.
——, A. Glazer, W. Szyrmer, G. Isaac, and I. Zawadzki, 1995: Forecasting of supercooled clouds. *Mon. Wea. Rev.,* **123,** 2093–2113.
Xu, Q., 1986: Conditional symmetric instability and mesoscale rainbands. *Quart. J. Roy. Meteor. Soc.,* **112,** 315–334.